Available online at www.sciencedirect.com
SCIENCE DIRECT®
PERGAMON
International Journal of Heat and Mass Transfer 46 (2003) 3017–3028
International Journal of HEAT and MASS TRANSFER
www.elsevier.com/locate/ijhmt

Numerical simulation of fuel sprays at high ambient pressure: the influence of real gas effects and gas solubility on droplet vaporisation

S. Hohmann [a], U. Renz [b,*]

[a] MTU Aero Engines GmbH, TESW, Dachauerstrasse 665, München 80995, Germany
[b] Lehrstuhl für Wärmeübertragung und Klimatechnik, RWTH Aachen, Eilfschornstrasse 18, Aachen 52056, Germany

Received 29 November 2001; received in revised form 2 January 2003

Abstract

This paper deals with the numerical simulation of the vaporisation of an unsteady fuel spray at high ambient temperature and pressure solving the appropriate conservation equations. The extended droplet vaporisation model accounts for the effects of non-ideal droplet evaporation and gas solubility including the diffusion of heat and species within fuel droplets. To account for high-temperature and high-pressure conditions, the fuel properties and the phase boundary conditions are calculated by an equation of state and the liquid/vapour equilibrium is estimated from fugacities. Calculations for an unsteady diesel-like spray were performed for a gas temperature of 800 K and a pressure of 5 MPa and compared to experimental results for droplet velocities and diameter distribution. The spray model is based on an Eulerian/Lagrangian approach. The comparison shows that the differences between the various spray models are pronounced for single droplets. For droplet sprays the droplet diameter distribution is more influenced by secondary break-up and droplet coagulation.

1. Introduction

Numerical methods for modelling spray formation and droplet evaporation in internal combustion engines and gas turbine combustors are mostly based on an Eulerian description of the gas phase conservation equations for momentum, energy, and species, and a Lagrangian description of the droplet phase [9,10]. Both phases are coupled by source terms in the conservation equations of the gas phase describing the transfer rates of momentum, energy and mass [4,37].

To further optimise the combustion process in particular to reduce the emission of NO_x and soot many processes occurring in the combustion chamber have to be studied in detail. These are the atomisation of the fuel at the nozzle and the penetration and vaporisation of the produced droplets, which govern the distribution of the fuel vapour in the combustion chamber. It is obvious that the fuel distribution has a strong influence on the emission formation in DI-diesel engines as well as in gas turbine combustors. The numerical simulation of these phenomena including the coupled transfer of momentum, heat and mass essentially supports the development process and optimisation of new engine concepts as it can partly replace time consuming and costly rig tests.

The trend toward higher combustion chamber pressures driven by the requirement of better specific fuel consumption was the reason to realise conditions for which the temperature and pressure in the gas phase are higher than the critical values of the liquid fuel. DI-diesel engines combustion pressures are typically above 5 MPa with gas temperatures of up to 900 K [21]. Similar ambient conditions were also realised for new technological concepts of aero engine gas turbine combustors [8].

It was already shown by several authors that beside non-ideal physical properties the solubility of the surrounding gas at the surface of the liquid droplet has to

* Corresponding author.
E-mail address: renz@wuek.rwth-aachen.de (U. Renz).

0017-9310/03/$ - see front matter © 2003 Elsevier Science Ltd. All rights reserved.
doi:10.1016/S0017-9310(03)00077-2

Nomenclature

B_m	mass transfer driving force
C_p	specific heat
C_D	drag coefficient
d	diameter
D	diffusion coefficient
M	molecular mass
$\dot{m}$	mass flux
N	number of moles
Nu	Nusselt number
p	pressure
Pe	Peclet number
$\dot{Q}$	heat flux
r	radius, radial co-ordinate
R	gas constant
Re	Reynolds number
Sc	Schmidt number
S	source term
Sh	Sherwood number
t	time
T	temperature
u	velocity, axial
v	velocity, radial
V	molar volume
$\underline{V}$	absolute volume
x	axial co-ordinate
Z	compressibility factor

Greek symbols

Δh_v	heat of vaporization
ε_i	normalised mass flux of component i
ϕ_i	fugacity
ϕ	general variable
Γ	general diffusivity
χ	correction for internal circulation
λ	heat conductivity
ρ	density
ψ	mole fraction
ξ	mass fraction
ω	acentric factor

Subscripts

c	critical
conv	convection
d	droplet
eff	effective
i	component i
h	heat
m	mass
g	gaseous
s	surface
0	without mass transfer
vap	vaporization
∞	infinity

be taken into account for the estimation of the phase equilibrium see e.g. [7,13,29]. These phenomena can be addressed by an equation of state. Furthermore, the diffusive transport processes inside the droplet, i.e. the heat conduction and the diffusive transport of liquid species, cannot be neglected as the surface of the droplet heats up faster than the core of the droplet [2,18]. The effective transport model according to Abramzon and Sirignano [1] for the mathematical description of the heat transport during the vaporisation process of single component droplets was extended for multi-component fuels [17]. The model, which uses effective transport parameters to account for the droplet internal circulation is now further extended to introduce real gas effects and gas solubility at the droplet surface as well as the diffusive transport of the dissolved gas inside the droplet. The numerical calculations for single droplets show a significant effect of the described phenomena.

The model has been implemented into the 3-D CFD code FLUENT for the calculation of unsteady sprays under high-pressure conditions [11]. The numerical results will be compared to experimental data from an unsteady fuel spray in a high-temperature–high-pressure chamber. The spray chamber equipped with a common rail injection system and a single hole nozzle has an inner diameter of 100 mm and a length of 150 mm [35]. Optical access is provided through several quartz windows. Detailed measurements with a phase Doppler anemometer (PDA) have been carried out and comparisons for calculated and measured droplet diameter distributions will be presented.

2. Description of the numerical model

A schematic of the physical processes occurring in DI-diesel sprays is shown in Fig. 1.

The transient injection process can be divided into several sub-processes. The liquid flow through the nozzle is followed by the primary atomisation of the liquid into filaments and drops [33]. In the near nozzle region, droplet collision and coagulation occur, as the number density of the droplets is very high. Due to the high relative velocity between the liquid drops and the surrounding gas secondary break-up can be induced. The atomisation process is followed by droplet vaporisation that is characterised by high heat and mass transfer rates. Starting from the modelling of the primary

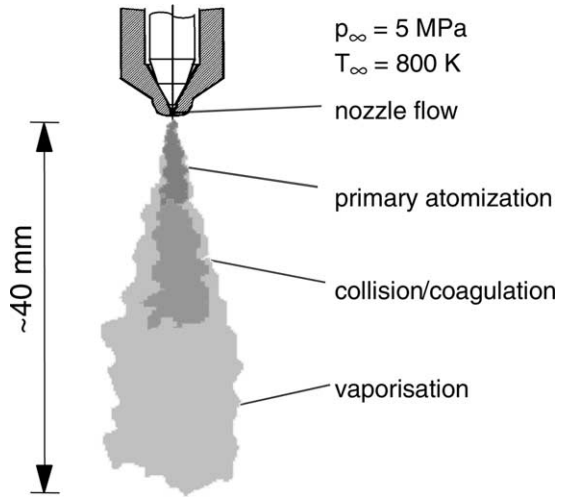

Fig. 1. Sub-processes in the spray.

atomisation at the nozzle [24,38], the trajectories of the droplets in the combustion chamber are calculated. The coupling of the two phases is accounted for by additional terms in the governing equations for the gaseous phase. The main emphasis of this paper is on the influence of the droplet vaporisation modelling on the spatial distributions of temperature and vapour concentration in the gas phase.

2.1. Gaseous phase

The unsteady, turbulent conservation equations for mass, momentum, energy, and species concentration have to be solved together with the liquid phase conservation equations. Since a single spray in an axis-symmetric pressure chamber is being investigated, the Reynolds-averaged gas phase equations are written in general cylindrical co-ordinate form as follows [28]:

$$\frac{\partial}{\partial t}(\rho\phi)+\frac{\partial}{\partial x}(\rho u\phi)+\frac{1}{r}\frac{\partial}{\partial r}(r\rho v\phi) = \frac{\partial}{\partial x}\left(\Gamma_\phi\frac{\partial\phi}{\partial x}\right)+\frac{1}{r}\frac{\partial}{\partial r}\left(r\Gamma_\phi\frac{\partial\phi}{\partial r}\right)+S_\phi \quad (1)$$

The general variable ϕ represents velocity component u, v, total enthalpy h_t, species ξ_1 and ξ_2 for the fuel components, and the turbulence quantities k and ε. These equations are solved using a finite-volume approach [9]. Momentum, heat and mass are transferred from the droplet phase to the gas phase thereby changing the velocity, temperature and vapour mass fraction fields. The source terms S_ϕ include the contributions due to momentum, energy and mass transferred from the liquid phase. Details can be found in [20,37].

2.2. Droplet vaporisation

To evaluate heat and mass fluxes at the droplet surface the gaseous boundary layer around the droplet is considered following the model of Abramzon and Sirignano [1]. From the integration of the quasi-steady species balance around the droplet follows an equation for the mass flux for each species:

$$\dot{m}_i=\varepsilon_i\dot{m}=\varepsilon_i\pi d_d(\rho D_i)_g Sh_i\ln(1+B_{m,i}) \quad (2)$$

The total mass flux is the sum of the individual species mass fluxes given by this equation. The Spalding number for the mass transfer $B_{m,i}$ is calculated as

$$B_{m,i}=\frac{\xi_{i,g,s}-\xi_{i,g,\infty}}{\varepsilon_i-\xi_{i,g,s}} \quad (3)$$

To account for surface blowing the film correction presented by Abramzon and Sirignano [1] is used.

$$Sh_i=2+\frac{Sh_{i,0}-2}{F(B_{m,i})} \quad (4)$$

The correction function F for the Spalding number B_i is given by the equation:

$$F(B)=(1+B)^{0.7}\frac{\ln(1+B)}{B} \quad (5)$$

This correction function also includes the effect of an enlarged boundary layer due to the Stefan flow. The Sherwood number is calculated by an empirical formula for spherical droplets:

$$Sh_0=2+0.6Re^{1/2}Sc^{1/3} \quad (6)$$

The mass fluxes for two components have to be calculated in addition to the overall mass flux as for a single component droplet. To account for different diffusion coefficients of the vaporising species in the gas an iterative procedure is applied to calculate the normalised mass fluxes ε_i of the two components. Details can be found in [16,17].

The heat penetrating into the liquid has to be specified as the boundary condition for the energy balance of the droplet. It is calculated according to Abramzon and Sirignano [1]:

$$\dot{Q}_l=\dot{Q}_{conv}-\dot{Q}_{vap}=\dot{m}\left[\frac{C_p(T_\infty-T_s)}{B_h}-\Delta h_v\right] \quad (7)$$

The Spalding number for heat transfer B_h is calculated from

$$B_h=\exp\left(\frac{\dot{m}C_p}{\pi d_d\lambda Nu}\right)-1 \quad (8)$$

Again, a correction for high mass transfer rates [1] is applied.

$$Nu = 2 + \frac{Nu_0 - 2}{F(B_h)} \tag{9}$$

This method to calculate the heat flux at the droplet surface is suitable for non-unity Lewis numbers. An empirical Nusselt formula for spheres is used:

$$Nu_0 = 2 + 0.6Re^{1/2}Pr^{1/3} \tag{10}$$

The assumption of a steady state boundary layer is used by many authors (i.e. [3,5,18,40]) to evaluate the heat and mass fluxes. It might be regarded as a rather crucial simplification but allows to account for the contribution of the convection by using empirical correlations for the *Nu* and *Sh* numbers. For spray calculations convective effects have to be taken into account.

2.3. High-pressure effects

The vapour mass fraction at the droplet surface has to be specified to calculate the mass transfer number $B_{m,i}$. For high-pressure conditions the assumption of ideal mixing behaviour is no longer valid and Raoult's law for the calculation of the vapour mass fractions at the droplet surface is not appropriate. To include the non-ideal behaviour in the gas phase and to account for gas solubility at the droplet surface the Peng Robinson (PR) equation of state [27] has been applied to estimate the vapour/liquid equilibrium:

$$p = \frac{RT}{V - b} - \frac{a(T)}{V(V + b) + b(V - b)} \tag{11}$$

The coefficients a and b for the pure components are calculated as follows [27]:

$$a(T) = 0.45724\frac{R^2T_c^2}{p_c}\left[1 + f\omega\left(1 - \left(\frac{T}{T_c}\right)^{1/2}\right)\right]^2 \tag{12}$$

$$f\omega = 0.37464 + 1.54226\omega - 0.26992\omega^2 \tag{13}$$

$$b = 0.07780\frac{RT_c}{p_c} \tag{14}$$

The critical values T_c, p_c and the acentric factor ω for the pure components are given in Daubert and Danner [6]. For mixtures, the coefficients a_m and b_m are calculated using mixing rules [32].

Defining the compressibility factor $Z = pV/RT$, the equation of state can be transformed into a cubic equation:

$$Z^3 - (1 - B^*)Z^2 + (A^* - 2B^* - 3B^{*2})Z - A^*B^* + B^{*2} + B^{*3} = 0 \tag{15}$$

with

$$A^* = \frac{a_m p}{R^2T^2} \tag{16}$$

$$B^* = \frac{b_m p}{RT} \tag{17}$$

For each component in the mixture the conditions of thermodynamic equilibrium is given by identical fugacities in the liquid droplet and the gaseous vapour phase:

$$(f_i)_d = (f_i)_g \tag{18}$$

To relate the fugacity to temperature and pressure it useful to introduce fugacity coefficients

$$\phi_i = \frac{f_i}{\psi_i p} \tag{19}$$

In this equation ψ_i are the mole fractions in the liquid droplet and the vapour phase and ϕ_i is the corresponding fugacity coefficient. The fugacity coefficients ϕ_i of each component in the liquid and the gaseous phase depend on pressure, temperature and composition. For an equation of state that is explicit in pressure the fugacity coefficients can be evaluated by:

$$RT\ln\phi_i = -\int_{\infty}^{\underline{V}}\left[\left(\frac{\partial p}{\partial N_i}\right)_{T,\underline{V},N_{j\neq i}} - \frac{RT}{\underline{V}}\right]d\underline{V} - RT\ln Z \tag{20}$$

For the PR-equation of state, the integration leads to the following expression, see [32]:

$$\ln\phi_i = \frac{b_i}{b}(Z - 1) - \ln(Z - B^*) + \frac{A^*}{2\sqrt{2}B^*} \times \left(\frac{b_i}{b} - \frac{2}{a}\sum_j \psi_j(a_i a_j)^{1/2}\right)\ln\left(\frac{Z + B^*(1 + \sqrt{2})}{Z + B^*(1 - \sqrt{2})}\right) \tag{21}$$

An iterative method is required to obtain the equilibrium mole fractions.

The enthalpy for the phase change of each component can be calculated from the fugacities:

$$\Delta h_{v,i} = -\frac{RT^2}{M_i}\frac{\partial}{\partial T}\left(\ln\frac{\phi_{i,g}}{\phi_{i,d}}\right) \tag{22}$$

The enthalpy for phase change and the surface tension vanish at the critical state. When droplets are approaching the critical state, the Weber number of the droplets, injected as a cold liquid, increases and it is commonly assumed that secondary break-up occurs prior the droplet surface gets critical. The present calculations support this assumption.

2.4. Droplet internal processes

The energy and species conservation equations for a binary droplet with variable properties, assuming spherical symmetry, can be written as follows, see e.g. [18] or [22].

Energy:

$$\frac{\rho_d C_p}{\lambda_d}\frac{\partial T_d}{\partial t} = \frac{\partial^2 T_d}{\partial r^2} + \left(\frac{2}{r} + \frac{1}{\lambda_d}\frac{\partial \lambda_d}{\partial r}\right)\frac{\partial T_d}{\partial r} \tag{23}$$

Species conservation:

$$\frac{\partial \xi_{i,d}}{\partial t} = D_{AB}\left[\frac{\partial^2 \xi_{i,d}}{\partial r^2} + \left(\frac{2}{r} + \frac{1}{\rho_d}\frac{\partial \rho_d}{\partial r} + \frac{1}{D_{AB}}\frac{\partial D_{AB}}{\partial r}\right)\frac{\partial \xi_{i,d}}{\partial r}\right] - \xi_{i,d}\frac{1}{\rho_d}\frac{\partial \rho_d}{\partial t} \tag{24}$$

The transport coefficients are modified according to the effective transport model proposed by Abramzon and Sirignano [1] to take into account the circulation inside the liquid droplet. The thermal conductivity λ_d and the diffusion coefficient D_{AB} are multiplied by a correction factor that depends on the liquid Peclet number:

$$\lambda_{d,eff} = \chi \lambda_d \tag{25}$$

$$D_{AB,eff} = \chi D_{AB} \tag{26}$$

$$\chi = 1.86 + 0.86 \tanh\left[2.245 \log_{10}\left(\frac{Pe_d}{30}\right)\right] \tag{27}$$

Under the present conditions the transport coefficients increase by a factor of approximately 2.7 compared with the purely diffusive properties.

Boundary conditions at the centre and at the surface of the droplet are as follows:

$r = 0$:

$$\frac{\partial T_d}{\partial r} = 0, \quad \frac{\partial \xi_{i,d}}{\partial r} = 0 \tag{28}$$

$r = r_d(t)$:

$$4\pi r_d^2 \lambda_d \frac{\partial T}{\partial r} = \dot{Q}_{conv} - \dot{Q}_{vap} \tag{29}$$

$$\rho_d D_{AB}\frac{\partial \xi_{i,d}}{\partial r} = \frac{\dot{m}}{4\pi r_d^2}(\xi_{i,d,s} - \varepsilon_i) \tag{30}$$

The boundary conditions at the droplet surface, describing the heat and mass transfer from the gas to the liquid, are the same for the well-mixed, the diffusion-limit and effective-diffusivity model.

When evaluating the heat and mass fluxes at the surface, the gaseous boundary layers around the droplet have to be considered. The heat and mass fluxes at the droplet surface have been given in Eqs. (2) and (7).

The conservation equations for heat and mass transfer inside the droplet were discretised on a non-dimensionalised spatial co-ordinate implicit in time. The resulting system of equations is solved using the tri-diagonal matrix algorithm [26,31] to evaluate the temperature and species concentrations within the droplet. A grid with 10 equally spaced grid points is a fair compromise between accuracy and computational effort for the coupled systems of the conservation equations.

2.5. Thermophysical properties

An important feature of the model is the evaluation of temperature and concentration dependent gas and liquid properties near the critical state. For the liquid phase, reduced temperatures are used to calculate the properties up to the critical temperature using the estimation techniques as recommended by Reid and Prausnitz [32] for the pure liquid properties and applying appropriate mixing rules for hydrocarbon components also taken from [32]. For the gaseous phase pure component properties the correlations given by Daubert and Danner [6] are used. The specific heat of the gaseous species is determined by assuming ideal gas behaviour. The influence of pressure is taken into account for the density and the diffusion coefficient. To calculate the heat and mass transfer rates the properties are evaluated using the 1/3-rule for temperature and mass fraction [12] and mixing rules as recommended by Reid and Prausnitz [32] are applied.

2.6. Droplet motion

The droplet trajectories are determined by integration of the particle equation of motion. The decrease of the velocity of the injected droplets is calculated from

$$\frac{du_d}{dt}\left(1 - 0.5\frac{\rho_\infty}{\rho_d}\right) = \frac{3}{4}\frac{\mu_\infty}{\rho_d d_d^2} Re C_D |u_g - u_d| \tag{31}$$

where u_g is the instantaneous gas velocity taken from a random walk model [9].

An empirical drag law is used which is valid for spherical particles and corrected for the friction loss due to evaporation [34].

$$C_D = \frac{24}{Re}(1 + 0.15 Re^{0.687})(1 + B_h)^{-0.2} \tag{32}$$

The Lagrangian method is employed to integrate the equation of motion.

2.7. Spray calculations

The model was implemented into a modified version of the finite-volume code FLUENT V4.4 [9] to solve the coupled equations for the gaseous and liquid phase for an unsteady spray under diesel engine conditions. For the calculation of the two-phase flow the Eulerian/Lagrangian scheme is used and the PSI-cell approach [4] is applied to calculate the source terms resulting from the interaction between the droplet phase and the gaseous phase. The stochastic behaviour due to the gas phase turbulence is accounted for by using a discrete eddy

concept [10,39] and the turbulent interaction time (eddy lifetime) is determined as given by Milojevic [23].

Time-dependent injection pressure measurements are used to calculate the liquid velocities at the nozzle exit. The initial droplet size distribution is determined from the atomisation model of Obermeier and Schneider [24,38] where it is assumed that small droplet are stripped from a liquid core due to aerodynamic shear forces.

As the present investigation focuses on a transient spray in a constant high-pressure environment, it is possible to pre-calculate the phase equilibrium with the high-pressure model as a function of temperature and liquid composition for the given fixed ambient pressure and to use look-up tables during the spray calculation. This method requires no additional computation time whilst including all non-ideal effects on phase equilibrium in the vaporisation calculation.

Spray calculations have been performed with the effective transport and the well-mixed models for the single component fuel *n*-heptane as well as for the binary model fuel D7N3, consisting of 70 vol% *n*-decane and 30 vol% α-methylnaphthalene.

3. Validation experiments

For isolated droplets data from literature [15,25,40] have been used to validate the evaporation model. For comparison of the spray modelling, detailed phase-Doppler measurements have been conducted in a high-temperature–high-pressure chamber [35]. The spray chamber equipped with a common rail injection system [41] and a single hole nozzle has an inner diameter of 100 mm and a length of 150 mm. Single injections have been repeatedly performed at a constant air velocity in the chamber of about 0.1 m/s that ensures reproducible boundary conditions in the gas phase for each single injection. A sketch of the experimental set-up is displayed in Fig. 2.

Optical access is provided through several quartz windows. For the PDA measurements a scattering angle of 65° has be chosen to minimise the error of variable refractive index of the evaporating droplets on the diameter measurement [19]. The arrangement of the PDA system and the chamber are shown in Fig. 3.

Detailed measurements of droplet velocities and droplet diameter distributions have been carried out for comparison with the numerical calculations.

4. Results and discussion

4.1. Isolated droplets

In order to validate the high-pressure model calculated results of the diameter evolution of isolated droplets in a high-pressure–high-temperature environment are compared with existing data.

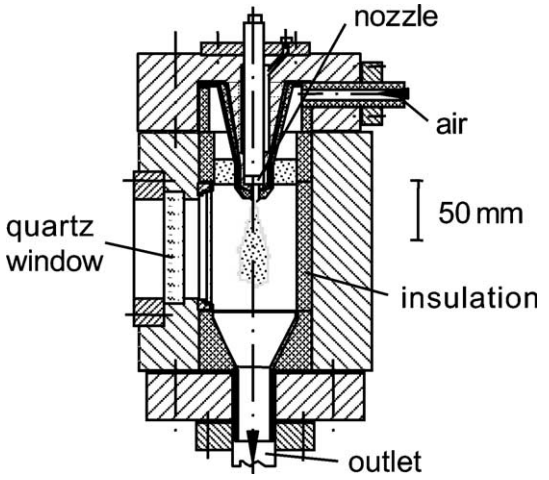

Fig. 2. High-pressure chamber.

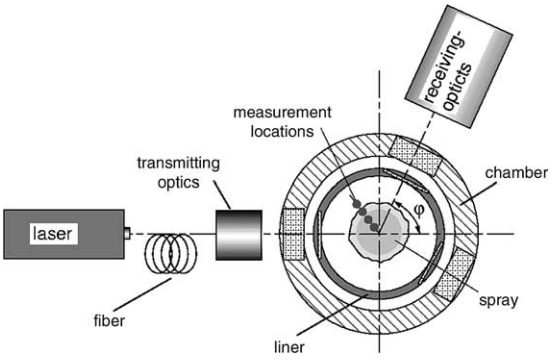

Fig. 3. Optical set-up of PDA system.

For high ambient pressures a noticeable amount of gas is dissolved at the droplet surface. Fig. 4 illustrates the high-pressure phase equilibrium of *n*-hexane and nitrogen for an ambient pressure of 6.89 MPa.

The lower line in this diagram represents the liquid composition, the upper one shows the composition in the gaseous phase which is in equilibrium with the liquid. Both curves approach each other when the critical state is reached. The mass fraction of nitrogen in the gas phase decreases with increasing temperature as the partial pressure of *n*-hexane rises. It is to mention that the mass fraction of dissolved gas in the liquid is in the order of 5%, nearly independent of temperature. Further investigations showed a similar behaviour also for other *n*-alkanes like pentane, heptane, decane or dodecane, the latter are often used as model fuels for diesel in IC engine calculations or kerosene for gas turbine combustor simulations.

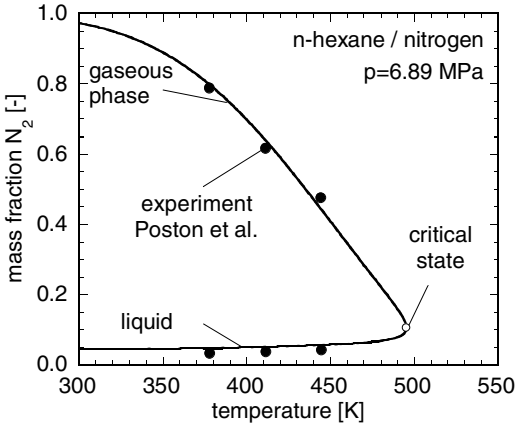

Fig. 4. Phase equilibrium of *n*-hexane/nitrogen system: comparison with data of Poston and McKetta [30].

From this behaviour it could be expected that the assumption of Raoult's law to estimate the vapour mass fraction at the droplet surface is rather rough and will lead to significant errors. In order to validate the high-pressure evaporation model a comparison with data of Kadota and Hiroyasu [15] and Olthoff [25] for suspended droplets evaporating in a stagnant atmosphere are presented in Fig. 5.

The normalised diameter evolution with time for suspended droplets with an initial diameter of $d_0 = 1.8$ mm evaporating in a stagnant nitrogen atmosphere is displayed for *n*-heptane and *n*-pentane. Although the droplet diameter is much larger than it is usually the case for spray applications in diesel engines this test case shows clearly the errors if ideal behaviour for the phase equilibrium is assumed to evaluate the surface concentrations and enthalpy for phase change.

In both cases only with the high-pressure model a reasonable agreement with the experimental data could be found. With the assumption of ideal behaviour too long vaporisation times are predicted. If an equation of state is used to calculate the phase equilibrium, higher mole fractions of the evaporation species in the gas phase are calculated due to non-unity fugacity coefficients at high pressures. The higher mass fraction in the gas phase evaluated by the high-pressure model leads to a higher mass transfer number B_m that finally results in shorter evaporation times. Secondly, the enthalpy for phase change from high-pressure model is smaller compared to the ideal case [13,14].

The reason for choosing a relatively low temperature of the gas phase of 373 K to validate the models is the fact that for high gas temperatures a noticeable amount of heat is conducted through the suspending device. There are some theoretical approaches to account for this heat conduction effect [15,25]. At high temperatures the heat conduction through the suspension is even higher than the heat transfer by convection. For this reason only boundary conditions were compared for which the heat conduction through the suspender is negligible. For smaller droplet qualitatively the same behaviour would be observed but no experimental data are available for a quantitative validation.

For a further validation of the vaporisation model a comparison with data for freely falling droplets in a high-temperature–high-pressure chamber measured by Stengele [40] is shown in Fig. 6.

The relative droplet diameter is displayed as a function of the falling distance in the observation chamber

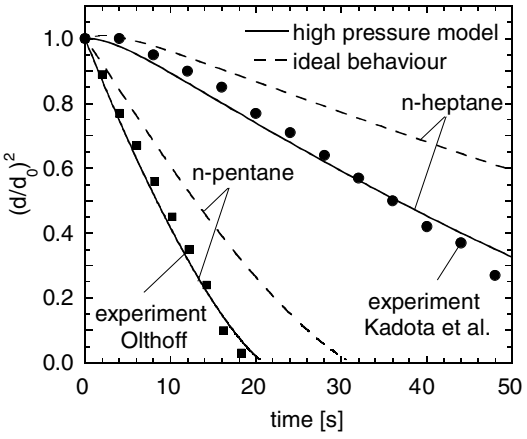

Fig. 5. Vaporisation of suspended single droplets ($d_0 = 1.8$ mm) at a temperature of 373 K and a pressure of 5 MPa. Comparison to data of Kadota and Hiroyasu [15] and Olthoff [25].

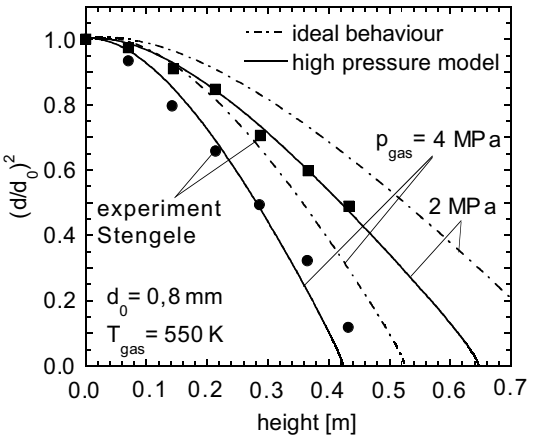

Fig. 6. Vaporisation of freely falling droplets at a temperature of 550 K and a pressure of 4 MPa. Comparison to data of Stengele [40].

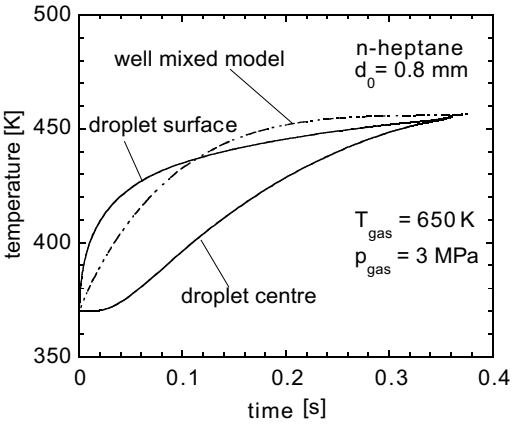

Fig. 7. Calculated droplet temperature histories.

for a droplet with an initial diameter of 0.8 mm at a temperature of 550 K and the pressures of 2 and 4 MPa. As could already be observed for stagnant droplets the evaporations rates predicted assuming ideal behaviour are too small and only with the high-pressure model a good agreement with the data can be achieved.

For high gas temperatures and high pressures the droplet internal transport processes become more important for the evaporation process. The effective transport model for which the one-dimensional enthalpy transport equation for the droplet is being solved can account for this behaviour. In Fig. 7 the evolution of the temperatures in the droplet centre and at the droplet surface are compared to the results of a calculation with the well-mixed model.

With the well-mixed model the temperature inside the droplet is uniform. The calculation with the effective transport model demonstrates that there are significant temperature gradients inside the droplet. At the beginning of the evaporation process the temperature at the droplet surface rises immediately, whereas the droplet centre remains at it's initial temperature. Due to the higher surface temperature in the initial phase, the mass transfer rate calculated with the effective transport model is higher compared to the well mixed model due to the higher partial pressure of the liquid at the surface.

The Biot number that characterises the ratio of external heat transfer to internal heat conduction should be small compared to unity to justify the application of the well-mixed model. For the specific conditions as displayed in Fig. 7 this is not the case. An evaluation of the Biot number results in a value of approximately $Bi = 2$ which shows that the external heat transfer is in the same order of magnitude as internal heat conduction. For higher gas temperatures this effect gets even more pronounced as the gaseous thermal conductivity usually increases with temperature and the liquid thermal conductivity decreases with temperature. As with higher gas pressures usually the droplet temperature also increases this effect is further enhanced.

Furthermore, the calculations show that in particular for the effective conductivity model there is no steady state surface temperature, which means that the process of liquid heating and evaporation is transient and the classical d^2-law is not applicable for the high-pressure conditions of a diesel engine (see also e.g. [36]).

To investigate the contribution of the internal diffusion of the dissolved gas a numerical experiment was carried out for droplets with boundary conditions comparable to the initial conditions of a transient diesel spray. The droplet diameter history was calculated for droplets with an initial diameter of 20 μm and an initial velocity of 100 m/s that evaporate in a stagnant atmosphere at a temperature of 800 K and a pressure of 5 MPa. These ambient conditions are comparable to DI-diesel engines or aero gas turbine combustion chambers.

In Fig. 8 calculated results with the high-pressure model are compared. For a single component fuel, it is possible to treat the droplet interior as a two-component mixture of liquid fuel and dissolved gas. The effective transport model accounts for the diffusive transport of both species inside the droplet. In the model "without gas transport" the high-pressure effects are included to predict the phase equilibrium but the diffusive transport inside the droplet is neglected.

Fig. 8 shows no significant difference for these two calculations with the high-pressure model, but if compared to the calculation with the assumption of an ideal behaviour, again one can observe much smaller vaporisation rates.

As already seen in Fig. 4 for equilibrium conditions the mass fraction of the dissolved gas at the droplet surface is in the order of 4–5%, depending on the liquid

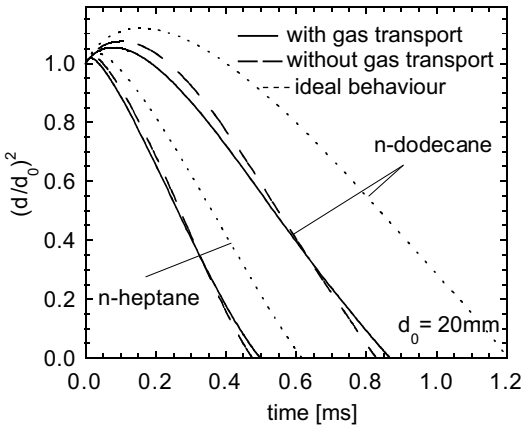

Fig. 8. Calculated diameter histories of *n*-heptane and *n*-dodecane droplets at $T = 800$ K and $p = 5$ MPa.

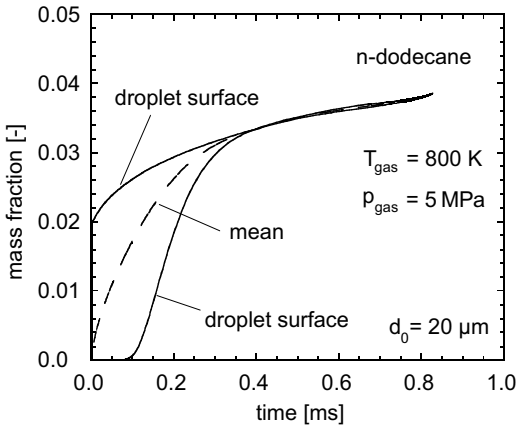

Fig. 9. Calculated mass fraction of dissolved gas within the droplet.

temperature. With the effective transport model it is possible to estimate the temporal evolution of the mass concentration of the dissolved gas inside the droplet. In Fig. 9, the mass concentration of the dissolved gas inside a 20 µm *n*-dodecane droplet is displayed for the droplet centre, the droplet surface together with the mean value.

Due to the equilibrium condition at the droplet surface the mass fraction immediately takes the value of the corresponding initial droplet surface temperature whereas the value at the droplet centre remains zero in the initial period. As can been seen, the concentration inside the droplet rises relatively fast and after less than half of the droplet lifetime the concentration of the dissolved gas inside the droplet is isotropic, but increases with time as the droplet temperature varies.

A question was, whether it is possible that an evaporating droplet may reach a pseudo-critical state at first in its interior, which would lead to a splashing from the inside. The present investigations do not show this effect for fuel droplets evaporating under conditions typical for DI-diesel or aero gas turbine combustion chambers. The fuel is initially injected as a cold liquid and after atomisation the drops evaporate in a high-temperature–high-pressure environment. The droplet temperature rises with time and the droplets are heated up from their surface to the interior. Also the concentration of the dissolved gas shows an analogous behaviour, higher values at the surface, lower value in the droplet interior. If a droplet should reach the critical state, this would occur at first in a region with high temperature and high concentration of dissolved gas, hence at the droplet surface. As already mentioned the surface tension vanishes if the critical state is reached, which means for a droplet in a highly turbulent flow field as in an DI-diesel spray, that secondary atomisation would occur immediately before the droplet gets critical.

4.2. Calculation of unsteady fuel sprays

To validate the initial and boundary conditions for the spray calculations, a comparison was carried out at first for an unsteady spray with weak droplet evaporation. A test case was selected for an ethanol spray injected into the pressure chamber with a temperature of $T = 600$ K and a gas pressure of 5 MPa. The injection pressure was 50 MPa in this case. In Fig. 10 mean droplets velocities measured in a plane 30 mm downstream the nozzle are compared to the numerical results. The measured time-dependent mean velocities were determined by PDA as an average over 1000 single injections of the fuel spray produced by the common-rail system. The mean value over these 1000 injections was calculated in time windows of 100 µs during the overall observation time of 2.5 ms from the start of injection.

After the spray reaches the measurement plane the mean velocities of the detected droplets increase immediately. Particularly at the spray axis a quasi-constant mean droplet velocity can be observed. At later times, after the end of the injection, the droplet velocities decrease again rather rapidly. This unsteady behaviour of the spray observed in the experiment can be well reproduced with the numerical model for the different radii in the spray. The position in time and the value of the maximum velocity compare very well. A number of calculations have been carried out and it has been observed that the evolution of the mean droplet velocities is nearly independent of their diameter, which leads to the conclusion that the result is mainly influenced by the exchange of momentum between the spray and the gas phase. Even though this comparison does not yet validate the droplet vaporisation model it demonstrates that the numerical procedure is well suited to capture the main features of this unsteady injection process.

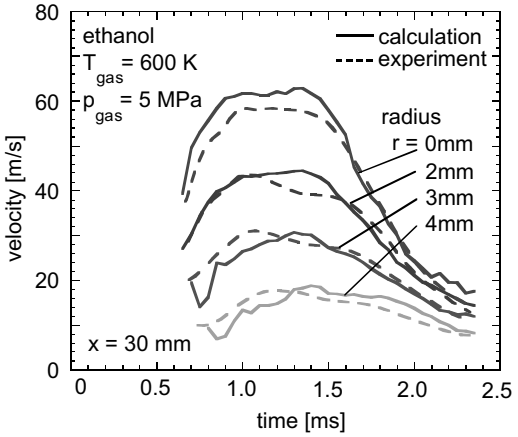

Fig. 10. Mean droplet velocities in a plane 30 mm downstream the nozzle.

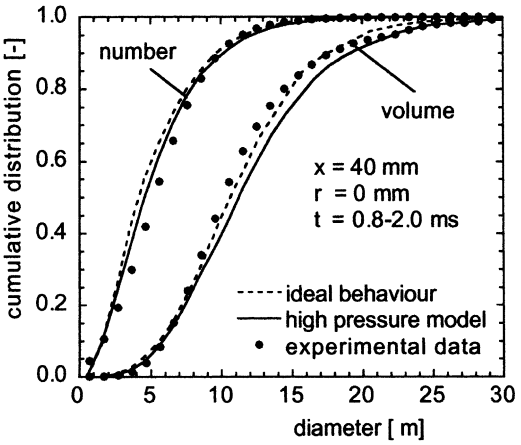

Fig. 11. Cumulative droplet number and droplet volume distribution on the spray axis 40 mm downstream the nozzle.

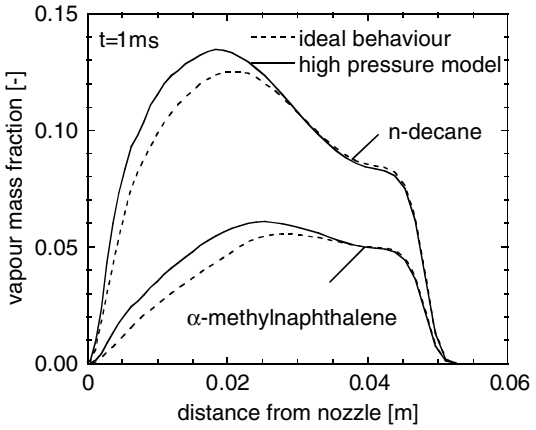

Fig. 12. Calculated vapour mass fractions for the model fuel D7N3.

For the further validation of the vaporisation model, calculated droplet diameter distributions are compared in Fig. 11 to the results of the PDA measurements for a strongly evaporating *n*-dodecane spray at a gas temperature of 800 K and a gas pressure of 5 MPa. The injection pressure was again 50 MPa. As was shown in Fig. 10 there is a time window of quasi-constant velocity particularly on the spray axis. This quasi-constant value over a longer time can also be observed for other spray variables like the mean diameter. This time window of quasi-constant velocity was selected for a comparison of the calculated droplet diameters to the measurements. The droplet diameter distribution was evaluated again as a mean over 1000 single spray injections, the time window for averaging was 0.8–2.0 ms after the start of injection.

Both, the calculated results with the high-pressure model and with the model assuming ideal behaviour for the droplet vaporisation compare well to the experimental data and only a weak dependence on the calculated results for the droplet diameter can be observed for the two calculations. The droplet diameter distributions calculated with the high-pressure model are slightly shifted to higher diameters which may be caused by the higher vaporisation rate that is predicted with this model, as already shown in the Figs. 6 and 8. The intensive evaporation process causes the smaller droplets to disappear faster, which results in a shift of the droplet diameter distribution to larger diameters.

For combusting sprays, the distribution of the gaseous fuel species in the combustion chamber is of particular interest as it significantly influences the emission formation. In numerical calculations very often the bi-component fuel D7N3 (70 vol% *n*-decane, 30 vol% α-methylnaphthalene) is used as a model fuel instead of diesel due to its rather similar vaporisation and ignition behaviour. Numerical results for the two vapour mass fractions along the spray axis are displayed for both vaporisation models in Fig. 12.

In this calculation the boundary conditions for the gas phase have been again a temperature of 800 K and a pressure of 5 MPa. The vapour mass fractions on the axis of the spray are shown for a time of 1 ms after the start of injection. As already observed for the single droplet calculations the higher vaporisation rate that is predicted with the high-pressure model leads to higher vapour mass fractions also for the spray calculations. The more volatile component *n*-decane evaporates much faster than the second component α-methylnaphthalene due to the difference in vapour pressure.

It can be concluded that the modelling of the droplet vaporisation has not that strong effect on spray evaporation as one would expect from the observations for isolated droplets due to the fact that many different physical processes interact within the spray, such as primary and secondary break-up, droplet collision and coagulation, exchange of momentum, heat and mass with the surrounding gas.

It was observed that the modelling of other subprocesses like secondary atomisation or droplet coagulation have a more pronounced influence on the droplet diameter which results in a strong effect on the predicted vapour concentration due to the direct dependence of the vaporisation rate on the droplet surface area. But the results of the vapour mass fraction, shown in Fig. 12, underline that the droplet vaporisation process should be modelled as exact as possible as the difference in predicted vapour concentration cannot be neglected.

5. Conclusion

For isolated droplets the numerical results using a high-pressure model show a significant pressure influ-

ence on the vaporisation rate. This behaviour could be observed for suspended droplets as well as for freely falling droplets. Good agreement was found comparing the numerical predictions with experimental data from literature. The calculations also show that the influence of additionally solving for the diffusive transport of dissolved gas within the droplet results only in a small effect on the predicted droplet histories.

Spray calculations are compared to own experimental data for single component fuels as *n*-docecane and ethanol and for two-component fuels measured in a high-pressure–high-temperature chamber. They show a good agreement for droplet velocity and the droplet diameter distributions.

Due to the fact that in dense fuel sprays the droplet diameter history is also influenced by secondary break-up and droplet coagulation the differences using either the high-pressure model or the model assuming ideal behaviour are not as pronounced as for isolated single droplets. In particular comparing the predicted vapour concentrations in the spray the differences between the well mixed and the effective transport model are small.

As the computational effort for the effective transport model is high and its influence on the predicted vapour concentration field is small, it is suggested that for spray calculations under DI-diesel or aero gas turbine conditions the well-mixed model together with look-up tables for the high-pressure phase equilibrium should be applied.

Acknowledgements

This work was supported by the Deutsche Forschungsgemeinschaft within the Graduiertenkolleg "Turbulenz und Verbrennung" and the Sonderforschungsbereich SFB 224 "Motorische Verbrennung".

References

[1] B. Abramzon, W.A. Sirignano, Droplet vaporisation model for spray combustion calculations, Int. J. Heat Mass Transfer 32 (9) (1989) 1605–1618.

[2] S.K. Aggarwal, Modelling of a dilute vaporizing multicomponent fuel spray, Int. J. Heat Mass Transfer 30 (9) (1987) 1949–1961.

[3] A.A. Amsden, KIVA-III: A KIVA program with block structured mesh for complex geometries, Los Alamos National Laboratory, 1993, LA-12503-MS.

[4] C.T. Crowe, M.P. Sharma, D.E. Stock, The particle–source-in-cell (PSI-cell) method for gas droplet flows, J. Fluids Engng. 99 (1977) 325–332.

[5] E.W. Curtis, P.V. Farell, A numerical study of high pressure droplet vaporisation, Combust. Flame 90 (1992) 85–102.

[6] T.E. Daubert, R.P. Danner, Physical and Thermodynamic Properties of Pure Chemicals: Data Compilation, Hemisphere Publishing Corporation, New York, 1989.

[7] J.-P. Delplanque, W.A. Sirignano, Numerical study of the transient vaporization of an oxygen droplet at sub- and supercritical conditions, Int. J. Heat Mass Transfer 36 (2) (1993) 303–314.

[8] M. Desaulty, Turbine engine combustor design, in: Proceedings of the 10th International Symposium on Air Breathing Engines (ISABE), Nottingham, GB, 1991.

[9] FLUENT Users Guide V 4.48, Fluent Inc., Centerra Resource Park, Lebanon, NH, USA, 1997.

[10] A.D. Gosman, E. Ioannides, Aspects of computer simulations of liquid-fuelled combustors, J. Energy 7 (6) (1983) 483–490.

[11] S. Hohmann, M. Klingsporn, U. Renz, An improved model to describe spray evaporation under diesel-like conditions, SAE Paper 960603, 1996.

[12] G.L. Hubbard, V.E. Denny, A.F. Mills, Droplet vaporisation: effects of transient and variable properties, Int. J. Heat Mass Transfer 18 (1975).

[13] H. Jia, G. Gogos, High pressure droplet vaporization: effects of liquid-phase gas solubility, Int. J. Heat Mass Transfer 36 (1993) 4419–4431.

[14] J.D. Jin, G.L. Borman, A model for multi-component droplet vaporization at high ambient pressures, SAE Paper 850264, 1985.

[15] T. Kadota, H. Hiroyasu, Evaporation of a single droplet at elevated pressures and temperatures, JSME Bull. 19 (138) (1976) 1515–1521.

[16] M. Klingsporn, U. Renz, Vaporisation of a binary unsteady spray at high temperature and high pressure, Int. J. Heat Mass Transfer 37 (Suppl. 1) (1994) 265–272.

[17] M. Klingsporn, Modellierung der Mehrkomponenten-Verdunstung bei der dieselmotorischen Einspritzung, Fortschritt-Berichte VDI Reihe 12, vol. 268, VDI-Verlag, Düsseldorf, 1996.

[18] R. Kneer, M. Schneider, B. Noll, S. Wittig, Diffusion controlled evaporation of a multicomponent droplet: theoretical studies on the importance of variable liquid properties, Int. J. Heat Mass Transfer 36 (1993) 2403–2415.

[19] R. Kneer, M. Willmann, M. Schneider, D. Hirleman, R. Koch, S. Wittig, Theoretical studies on the influence of refractive index gradients within multi-component droplets on size measurements by phase-Doppler anemometry, in: Proceedings of the 6th International Conference on Liquid Atomisation and Spray Systems (ICLASS), Rouen, 1994, pp. 451–458.

[20] G. Kohnen, M. Rueger, M. Sommerfeld, Convergence behaviour for numerical calculations by the Euler/Lagrange method for strongly coupled phases, Numer. Meth. Multiphase Flows, ASME FED 185 (1994) 191–202.

[21] K. Krieger, Einspritztechnik für PKW-Motoren-Überblick über Verfahren und Ergebnisse, MTZ 60 (5) (1999).

[22] R.B. Landis, A.F. Mills, Effect of internal diffusional resistance on the evaporation of binary droplets, in: Proceedings of the 5th International Heat Transfer Conference, Tokyo, Japan, Paper B7.9, 1974, pp. 345–349.

[23] D. Milojevic, Lagrangian stochastic–deterministic (LSD) predictions of particle dispersion in turbulence, Part. Part. Syst. Charact. 7 (1990) 181–190.

[24] F. Obermeier, MPI für Strömungsforschung, Göttingen, Model development within the CEC programme JRC-IDEA, 1993.
[25] P. Olthoff, Modellierung des Tropfenverdunstungsprozesses bei überkritischem Umgebungsdruck, Ph.D. Thesis, Universität Braunschweig, Germany, 1994.
[26] S.V. Patankar, Numerical Heat Transfer, Hemisphere Publishing Corporation, New York, 1980.
[27] D.Y. Peng, D.B. Robinson, A new two constant equation of state, Ind. Engng. Chem. Fundam. 15 (1976) 59–64.
[28] Joel H. Ferziger, Milovan Peric, Computational Methods for Fluid Dynamics, third ed., Springer-Verlag, Berlin, Germany, 2001.
[29] F. Poplow, Numerical calculation of the transition from subcritical droplet evaporation to supercritical diffusion, Int. J. Heat Mass transfer 27 (3) (1994) 485–492.
[30] R.S. Poston, J.J. McKetta, Vapour–liquid equilibrium in the *n*-hexane nitrogen system, J. Chem. Engng. Data 11 (1966) 364–365.
[31] W.H. Press, S.A. Teukolsky, W.T. Vetterling, B.P. Flannery, Numerical Recipes in Fortran, second ed., Cambridge University Press, Cambridge, 1992.
[32] R.C. Reid, J.M. Prausnitz, B.E. Poling, The Properties of Gases and Liquids, fourth ed., McGraw-Hill, New York, 1987.
[33] R.D. Reitz, F.V. Bracco, Mechanisms of atomization of a liquid jet, Phys. Fluids 25 (10) (1982) 1730–1742.
[34] M. Renksizbulut, R.J. Haywood, Transient droplet evaporation with variable properties and internal circulation at intermediate Reynolds numbers, Int. J. Multiphase Flows 14 (2) (1988) 189–202.
[35] U. Renz, A. Breuer, M. Klingsporn, Strahlausbreitung und Tropfenverdampfung bei der dieselmotorischen Einspritzung, Kolloquium des Sonderforschungsbereichs SFB 224, Motorische Verbrennung, RWTH Aachen, 1993.
[36] D.E. Rosner, W.S. Chang, Transient evaporation and combustion of a fuel droplet near its critical temperature, Combust. Sci. Technol. 7 (1973) 145–158.
[37] M. Rüger, S. Hohmann, M. Sommerfeld, G. Kohnen, Euler/Lagrange calculation of turbulent sprays: The effect of droplet collisions and calescence, Atomization Sprays 10 (2000) 47–81.
[38] T. Schneider, Zur Modellierung der Zerstäubung von Flüssigkeitsfreistrahlen, Dissertation Universität Dortmund, Germany, 1995.
[39] J.S. Shuen, L.-D. Chen, G.M. Faeth, Evaluation of a stochastic model of particle dispersion in a turbulent round jet, AIChE J. 29 (1) (1983) 167–170.
[40] J.F. Stengele, Tropfenverdunstung in Hochdruckatmosphäre, Dissertation, Universität Karlsruhe, Germany, 1998.
[41] G. Stump, M. Ricco, Common rail—An attractive fuel injection system for passenger car DI diesel engines, SAE Paper 960870, 1996.